THE JOURNAL OF PHYSICAL CHEMISTRY C

Article

pubs.acs.org/JPCC

Efficient Inverted Polymer Solar Cells with Directly Patterned Active Layer and Silver Back Grating

X.H. Li, Wei E.I. Sha, Wallace C.H. Choy,* Dixon D. S. Fung, and F. X. Xie

Department of Electrical and Electronic Engineering, The University of Hong Kong, Pokfulam Road, Hong Kong, China.

ABSTRACT: We have investigated the effects of a directly patterned active layer together with silver nanograting arrays as the anode of inverted polymer solar cells (PSCs). The patterned nanostructure not only greatly enhances the light absorption of the active layer through both light diffraction and coupling to surface plasmon polariton (SPP) modes but also obviously promotes the fill factor of the patterned device. The absorption spectrum shows improvement over a broad wavelength range, especially around the 400 nm region and the near-infrared region surrounding 700 nm, which can also be reconfirmed from Incident Photon to Electron Conversion Efficiency (IPCE) and zeroth-order reflection spectra. Most importantly, our physical study shows that the absorption peak of 400 nm is due to the resonant waveguide mode, and the absorption peak of 700 nm is attributed to the excited SPP mode induced by the metallic back grating. Besides, another splitting SPP mode, called plasmonic band edge, around 800 nm is clarified from our detailed model. Consequently, on one hand, our work offers the fundamental physical understanding of plasmonic band edge resonances in periodic grating nanostructures for enhancing the optical absorption of thin-film photovoltaics. On the other hand, the study contributes to improving the power conversion efficiency of inverted PSCs by about 19% through incorporating grating structures that can be a potential candidate for improving the performances of other PSCs.

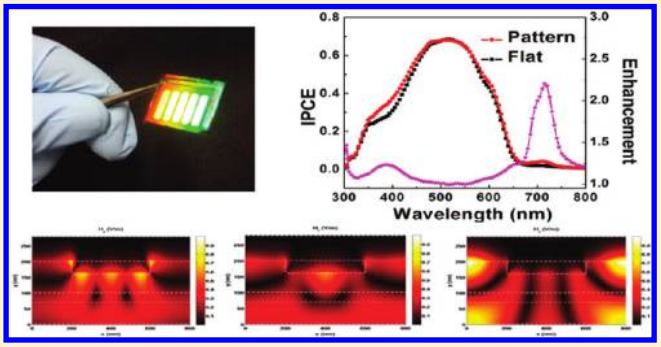

INTRODUCTION

Bulk heterojunction (BHJ) polymer solar cells (PSCs) have attracted attention due to their potentials as renewable energy sources.[1−4] Two main types of architectures are commonly adopted in PSCs.[5,6] The traditional device architecture comprises a transparent conducting metal oxide coated with a poly(3,4-ethylenedioxythiophene):poly(styrenesulfonate) (PEDOT:PSS) hole-transporting layer followed by the BHJ active layer and, finally, a low-work function electron-collecting metal electrode. The ITO/PEDOT:PSS/active layer/LiF/Al or Ca/Al is the most common and representative example of this structure.[5,6] The second architecture is the inverted structure, which replaces EDOT:PSS at the ITO interface by relatively air-stable and high-work function metal electrodes as the top electrode.[7,8] Meanwhile, metal anodes such as the Ag anode can be formed using coating or printing technology to simplify and lower the cost of manufacturing.[6] Consequently, the inverted architecture has recently drawn significant attention. However, inverted solar cells typically have lower power conversion efficiency (PCE) than the conventional structure.[6,9] Thus, it is highly desirable to further improve the performances of inverted PSCs to fully exploit their advantages.

Various methods have been reported in enhancing the performance of inverted PSCs, such as synthesizing new, efficient photoactive materials,[1,10,11] tailoring interfaces,[12,13] and developing light-trapping systems.[14−24] Improving light harvesting in the 600−900 nm wavelength range, where typical photoactive materials have a weak absorption region, is one of the promising pathways to increase PCE.[15,18,25−27] Recently, metallic nanostructures have been incorporated into PSCs to enhance light harvesting by light-scattering mechanism and strong surface plasmon polariton (SPP) effects.[14,28−32] However, there have been very limited studies on the inverted solar cells with directly patterned active layer and metallic nanograting electrode.

Although nanostructured back reflectors can improve the absorption of the active layer, the researchers integrated a nanoscale pitch back grating electrode with a traditional PSC device structure resulting in a reduced fill factor (FF) compared to the corresponding flat structure.[28,29,31,33] This is mainly because the traditional devices commonly use LiF/Al as the cathode. After the grating structure is fabricated on the active layers, the nonuniform distribution of thin LiF (commonly ∼1 nm) (on the grating surface) leads to a nonohmic cathode contact.[28,31,33] In the case of a Ca/Al cathode, the thick Ca (40 nm) will restrain the optical effect of Al.[29] These issues will be resolved by our inverted device structures in which both the optical absorption and FF improve.

Regarding periodic metallic gratings, most works[21,23] contributed the excitation of SPPs to one of Bloch mode with the momentum matching the condition of $k_{spp} = k_0 \sin\theta + (2\pi/P)n$, where k_{spp} is the dispersion relation of the SPP

Received: November 22, 2011
Revised: February 27, 2012
Published: March 13, 2012

supported in a semi-infinite metal/dielectric interface; k_0 is the wavenumber of free space; P is the periodicity of the grating; and n is the order of the Bloch mode. However, the predicted SPP enhancement peaks by the momentum matching condition deviate from the observed ones in a class of grating nanostructures with deep troughs. Wang et al.[34] observed the offsets in Ag nanogratings for thin-film silicon-based solar cells. However, no detailed physical explanations were provided. Bai et al.[35] theoretically investigated silicon-based solar cells for which SPPs occur not only on the upper surfaces but also at the bottom interfaces of gratings, albeit without specific physical understandings. In this work, we (1) find that the two phenomena previously reported are rooted in an identical physical origin called plasmonic band edge resonances. We (2) experimentally demonstrate the existences of the plasmonic band edge and plasmonic band gap in PSCs with Ag metallic nanogratings, (3) discuss their roles in improving the optical absorption of PSCs, and more importantly, (4) clarify their physical origins with our detailed study.

In this article, we report that both the SPP and diffraction effects can be explored to improve light trapping and PCE of inverted PSCs by fabricating a 2D nanoscale grating of active layer and plasmonic Ag anode through the PDMS nanoimprint method (see the Experimental Section and Figure 1a).

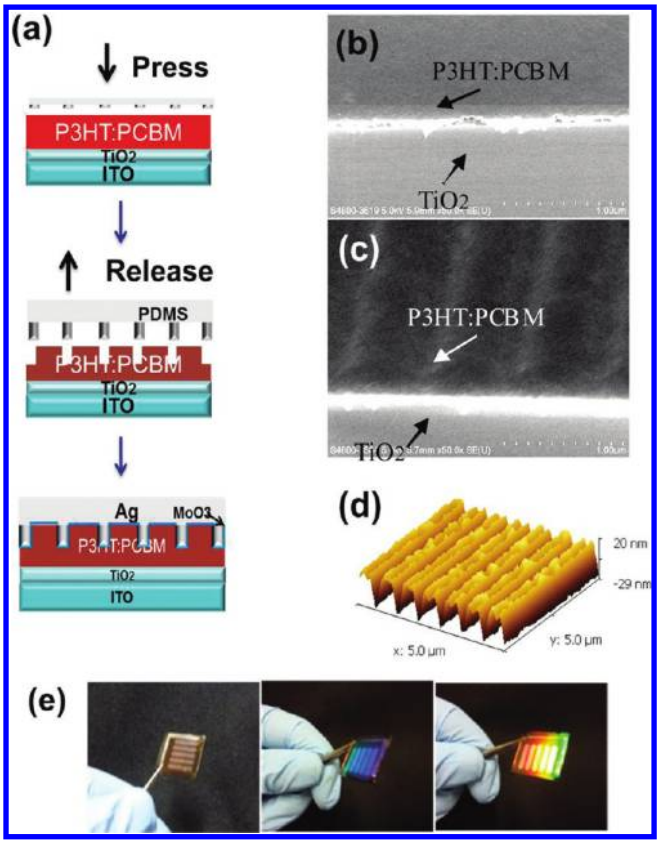

Figure 1. (a) Schematic fabrication sequence for the inverted solar cells with grating formed by a soft nanoimprinted approach. The graphic structure of the grating polymer solar cell ITO (70 nm)/TiO_2 (30 nm)/P3HT:PCBM grating/MoO_3 (8 nm)/Ag grating (80 nm). (b) 45°-tilt SEM image of the flat P3HT:PCBM film. (c) 45°-tilt SEM image of the P3HT:PCBM film with grating structure. (d) Atomic force microscopy (AFM) images of the P3HT:PCBM grating with the period of 750 nm and depth of 40 nm. (e) Photographs of a patterned device irradiated under several indoor daylight lamps at different tilted angles.

Our experimental and theoretical results show that the nanostructured Ag anode enhances the absorption of the active layer over a broad wavelength range. For the strong enhancements in the long wavelength region, theoretical studies have been conducted to understand the detailed physics as the four points described above. Consequently, our results show that incorporation of the Ag grating on a poly(3-hexylthiophene) (P3HT):[6,6]-phenyl-C61-butyric acid methyl ester ($PC_{60}BM$) inverted cell increases short circuit current density (J_{sc}) and FF and thus PCE by ~19%.

EXPERIMENTAL SECTION

Device Fabrication. Devices with structure of ITO/TiO_2 (30 nm)/active layer/MoO_3 (8 nm)/Ag (with or without grating) (80 nm) were fabricated by using the PDMS nanoimprinted method (Figure 1a). ITO glasses were cleaned based on a standard procedure. A thin layer (30 nm) of TiO_2 was obtained on the ITO after spin-coating. TiO_2 was synthesized from a nonhydrolytic sol–gel approach.[36] After stirring a solution of $TiCl_4$, ethanol, and benzyl alcohol for 3 h at 80 °C, it was washed with diethyl ether. The white TiO_2 precipitate was obtained by centrifuging the crude product. The final TiO_2 solution was prepared by dispersing it in ethanol. These samples were then dried at 150 °C for 30 min. Subsequently, polymer solution of poly(3-hexylthiophene) (P3HT):[6,6]-phenyl-C61-butyric acid methyl ester ($PC_{60}BM$) (1:0.8, w/w, 18 mg/mL) in chlorobenzene was spin-coated at 700 rpm for 60 s on top of the TiO_2 layer. The active layer thickness is about 100 nm.

To ensure the easy release of the replica with high reproducibility in the nanoimprinted process, we used flexible PDMS as an elastomeric mold for conformal contact with the substrate. PDMS, prepared by mixing an oligomer (Silard 184, Dow corning) and a curing agent (10:1, v/v), was poured onto the nanograting master. After removing the air bubbles and thermally curing at 79 °C for 3–4 h, PDMS stamps were obtained in which the grating of the periodic nanostructures corresponded to the dimension of the master grating. To inscribe the pattern on the active layer, the PDMS mold with replicated pattern from the Si master was put in conformal contact with the active layer. The PDMS mold was kept in nitrogen for 7 min during the annealing process, which was performed at 130 °C to enhance the degree of polymer ordering. After removed of the PDMS mold, MoO_3 (8 nm) and silver (80 nm) layers were thermally evaporated onto the active layer with pattern, in a vacuum at 10^{-6} Torr.

Characterization of Solar Cells and Thin Films. The thickness of the polymer sample was measured using a Dektak alpha-step profiler. The morphology of the sample was characterized using atomic force microscopy (AFM) (Asylum Research MFP-3D) in tapping mode and scanning electron microscopy (SEM) (Hitachi S-4800). The-zeroth order reflection spectra were experimentally determined by using a VASE ellipsometer from J.A. Woollam Co., Inc. The current density (J)–voltage (V) characteristics and Incident Photon to Electron Conversion Efficiency (IPCE) were also measured by using the methods described elsewhere.[20]

Theoretical Modeling. To theoretically investigate the optical properties of the PSC, we employed the finite-difference frequency-domain (FDFD) method to rigorously solve Maxwell's equations.[26] In our model, complex couplings or hybridizations between surface plasmon polariton (SPP) and Bloch modes supported in the metallic grating nanostructure have been fully taken into account. The near-field distribution

and absorption enhancement factor of PSCs with the metallic grating can be obtained by the FDFD method. In addition, the rigorous coupled-wave algorithm (RCWA) was used to access the zeroth-order reflection spectra.[37]

RESULTS AND DISCUSSION

A PDMS nanoimprinted method is applied to produce a plasmonic back reflector that features a 2D array of nanoscale Ag grating (Figure 1a). Before any pattern applied to the PSCs, the surface of the P3HT:PCBM blended active layer is generally smooth as shown in Figure 1b. After applying the pattern, we can clearly observe the grating features in Figures 1c and 1d. It should be noted that the lateral wall of the grating is not fully vertical, and this is beneficial for the subsequent coverage of MoO_3. When the anode (MoO_3 and Ag) is subsequently evaporated on the nanostructured active layer surface, the anode/active layer interface will closely follow the surface profile of the active layer. Hence, the grating features will be preserved on the Ag anode. The colorful reflection shown in Figure 1e is caused by the diffraction of Ag grating replica, which strongly depends on the periodicity, refractive index of the film, and the view angle.

The performances of PSCs with the structure of ITO/TiO_2/P3HT:PCBM/MoO_3/Ag without (control device) and with grating are investigated. Current density−voltage (J−V) characteristics of the representative devices are shown in Figure 2.

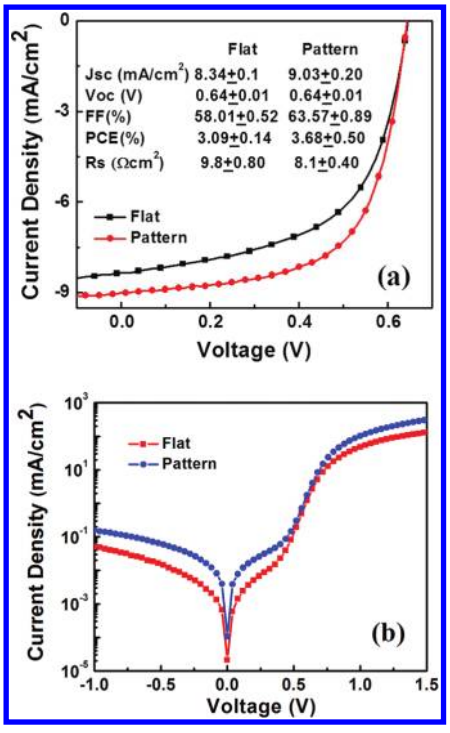

Figure 2. Current density−voltage (J−V) characteristics of devices with or without grating structure under (a) AM 1.5 illumination and (b) dark condition. Inset: Summary of the performance parameters of the flat and grating devices.

From the inset table of Figure 2a, we can see that the PCE of the device with grating obviously improves from 3.09% (control device) to 3.68% (grating device). PCE improvements are attributed to J_{sc} improvement from 8.34 to 9.03 mA/cm^2 and FF improvement from 0.580 to 0.635. The higher FF is a consequence of the nanoimprinted pattern increasing the interface area.[38] Besides, the series resistance of the devices decreasing from 9.8 Ω cm^2 (without grating) to 8.1 Ω cm^2 (with grating) is also a cause for a higher FF.[30] It is worth mentioning here that previous studies on grating structured Al electrode in conventional devices show that the grating either has no effect on or reduces FF. For example, Chaudhary et al. attributed the improvement of PCE of the device with textured substrates only to light-trapping rather than electrical effects.[28] Kim et al. fabricated the device with the structure of ITO/PEDOT:PSS/P3HT:PCBM/Ca (40 nm)/Al (with grating) and found that the FF of cells with grating depth of 40 nm decreased, which is due to the large thickness modulation of the grating structure.[29] Besides, the Ca layer of 40 nm thickness will prohibit the plasmonic effect from the rear Al electrode.[31,38] We tackle this issue by utilizing an inverted structure and carefully tuning the thickness of MoO_3 to obtain the most pronounced plasmonic effects. Through a series of experiments tuning the thickness of MoO_3, we find that the device exhibits an increased J_{sc} and decreased FF when the thickness of MoO_3 is below 5 nm (FF decrease ∼9% for 4 nm). This is because the depth of grating is about 40 nm, and a MoO_3 layer thinner that 5 nm may not fully cover the whole surface of the active layer, resulting in a nonohmic anode contact with low FF (∼0.53). The optimized structure uses 8 nm MoO_3, with which we simultaneously obtained an increased FF and a pronounced plasmonic effect. It should be noted that the MoO_3 thickness is relatively thin compared to the grating depth (∼40 nm). This is likely because the lateral wall of the grating is not fully vertical to the horizontal plane (see Figure 1d), so we could effectively cover the surface of the active layer with a relatively thin layer of MoO_3.

To understand the origin of the J_{sc} increment, we have measured the IPCE spectra of the devices (see Figure 3a). The

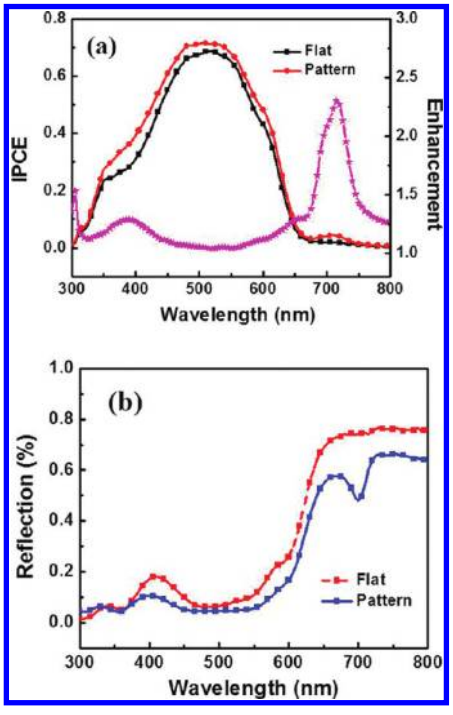

Figure 3. (a) IPCE of the devices with and without grating structure. (b) Zeroth-order UV−vis reflection spectra of the devices.

IPCE increases over the whole wavelength range particularly in the region of 380−550 nm. Moreover, there is a significant enhancement around ∼715 nm where P3HT does not absorb strongly. We have measured the zeroth-order reflection spectra

dx.doi.org/10.1021/jp211237c | J. Phys. Chem. C 2012, 116, 7200−7206

of both patterned and nonpatterned devices at normal incidence. According to the Figure 3b, the reflectance of the patterned device is reduced over a wide range from ~400 to 800 nm. Interestingly, large decreases in reflectance are observed at ~420 nm and ~715 nm after fabricating the grating on the device. These decreases in reflectance correspond to improved absorption in the active layer. Comparing the IPCE and reflectance plots (Figure 3a and Figure 3b), we can observe that the wavelength regions where reflectance decreases agree very well with the regions where IPCE increases. To further clarify our data, we calculated the ratio between the IPCE of devices with and without grating (see Figure 3a) and observed distinct peaks at ~400 nm and ~715 nm where reflectance decreases drastically. To elucidate physical origins for these absorption peaks, we rigorously solve Maxwell's equations governing optical properties of PSCs by using the finite-difference frequency-domain (FDFD) method. According to our theoretical results, the absorption peak of 400 nm is due to the excitation of waveguide mode as shown in Figure 4, which can be characterized by the

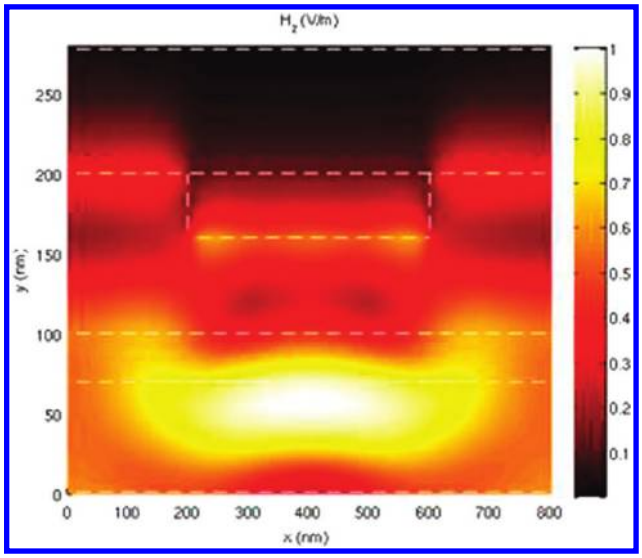

Figure 4. Waveguide model at around wavelength 400 nm.

generalized reflection coefficients method we have developed.[39] The broadband enhancement in the wavelength range of 380–550 nm can be achieved because the light path is elongated or diffracted by the grating nanostructure.[40,41]

Figure 5(a) shows the absorption enhancement of the PSC by the metallic grating for the TM wave at vertical incidence. Apart from the broad enhancement over 380–550 nm, the significant enhancement peaks of 1 and 3 as well as a dip of 2 can be clearly observed. Furthermore, the enhancement peak at ~710 nm correlates well with the position of the enhancement peak of IPCE at ~715 nm. However, in this case, the results of peak 1 and 3 cannot be explained with grating diffraction effects. Hence, we apply the rigorous FDFD model and mode coupling theory to understand these results. Figure 5(b) illustrates the corresponding near-field distributions. The concentrated near-field and charge distribution are mainly located at the peak and trough of the metallic grating, respectively, at 710 and 800 nm (relates to plasmonic band edges). Moreover, one can notice that the near field becomes suppressed at 760 nm (relates to plasmonic band gap). The intriguing phenomena strongly resemble those in photonic crystal (PC) occurring at band edges and the band gap. For PCs, forward and backward traveling waves constructively interfere with each other, resulting in standing waves. Due to the Bragg scattering in periodic photonic structures with modulated refractive indices, the degenerate standing waves split into two band edge modes with field concentrations in different regions. Between band edge frequencies, a band gap will be opened up due to the destructive interferences of traveling waves. Although it is nonintuitive that the phenomena could happen in metallic structures, no physical law forbids their existences.

Critically different from traveling waves in PCs, forward and backward SPP waves (animations of the 710 and 800 nm field profiles are available for download from the link in reference 42) constructively interfering with each other induce two plasmonic band edges with splitting resonance frequencies, which is due to the periodically modulated refractive indices of metallic grating structures. The plasmonic band edge resonance plays an important role in improving the optical absorption of PSCs as shown in the peaks of enhancement factor of Figure 5(a). To clarify the physical origin of the plasmonic band edge, we theoretically study the overlap integral between the near-field distribution of plasmonic band edges as shown in Figure 5(b) and Bloch modes of mth diffraction order. From the overlap integral, we can understand how the photon can be coupled to SPP and how Bloch modes hybridize SPP modes. The 2-D TM wave can excite the SPP, and thus the definition of the overlap integral is given by

$$Z = \left| \int_0^P \int_{y_b}^{y_p} H_z(x, y) \exp[ik_x x + ik_y(y - y_p)] \mathrm{d}x\mathrm{d}y \right| \tag{1}$$

$$k_x = k_0 \sin\theta + \frac{2\pi}{P} n,\ n = 0, \pm 1, \pm 2, \ldots,\ k_x^2 + k_y^2 = k_d^2$$

where P is the periodicity of the grating; y_b is the boundary between P3HT:PCBM and TiO_2 layers; y_p is the grating peak; $\theta = 0$ is the incident angle; n is the diffraction order; and k_0 and k_d are wave numbers of free space and P3HT:PCBM, respectively. Because the SPP is decayed away from the Ag/P3HT:PCBM interface, the sign of k_y should be selected for guaranteeing $\mathrm{Im}(k_y) < 0$. Here, the integral domain is limited to the P3HT:PCBM active layer below the metallic grating peak as shown in Figure 5(b) because the analytical forms of Bloch modes are known in this region. Figure 5(c) shows the normalized overlap integral at plasmonic band edges of 710 and 800 nm. From simple calculation ($\mathrm{Re}(k_d) > 2\pi/P$), we know the zeroth- and first-order Bloch modes are radiative modes related to incident wave, specula reflection, etc. They are not responsible for the excitation of SPPs. Moreover, the overlap integral values become very small when the diffraction order $|m| > 3$. Hence, the interplay between second- and third-order Bloch modes strongly affects the excitation of SPPs. At 800 nm (one of enhancement factor peak), the maximum in the overlap integral corresponds to second-order Bloch mode, which is much larger than that corresponding to third-order Bloch mode. The momentum matching condition of SPP in a periodic structure can be written as

$$k_{spp} = k_0 \sin\theta + \frac{2\pi}{P} n \tag{2}$$

$$k_{spp} = k_0 \sqrt{\frac{\varepsilon_m \varepsilon_d}{\varepsilon_m + \varepsilon_d}} \tag{3}$$

dx.doi.org/10.1021/jp211237c | J. Phys. Chem. C 2012, 116, 7200–7206

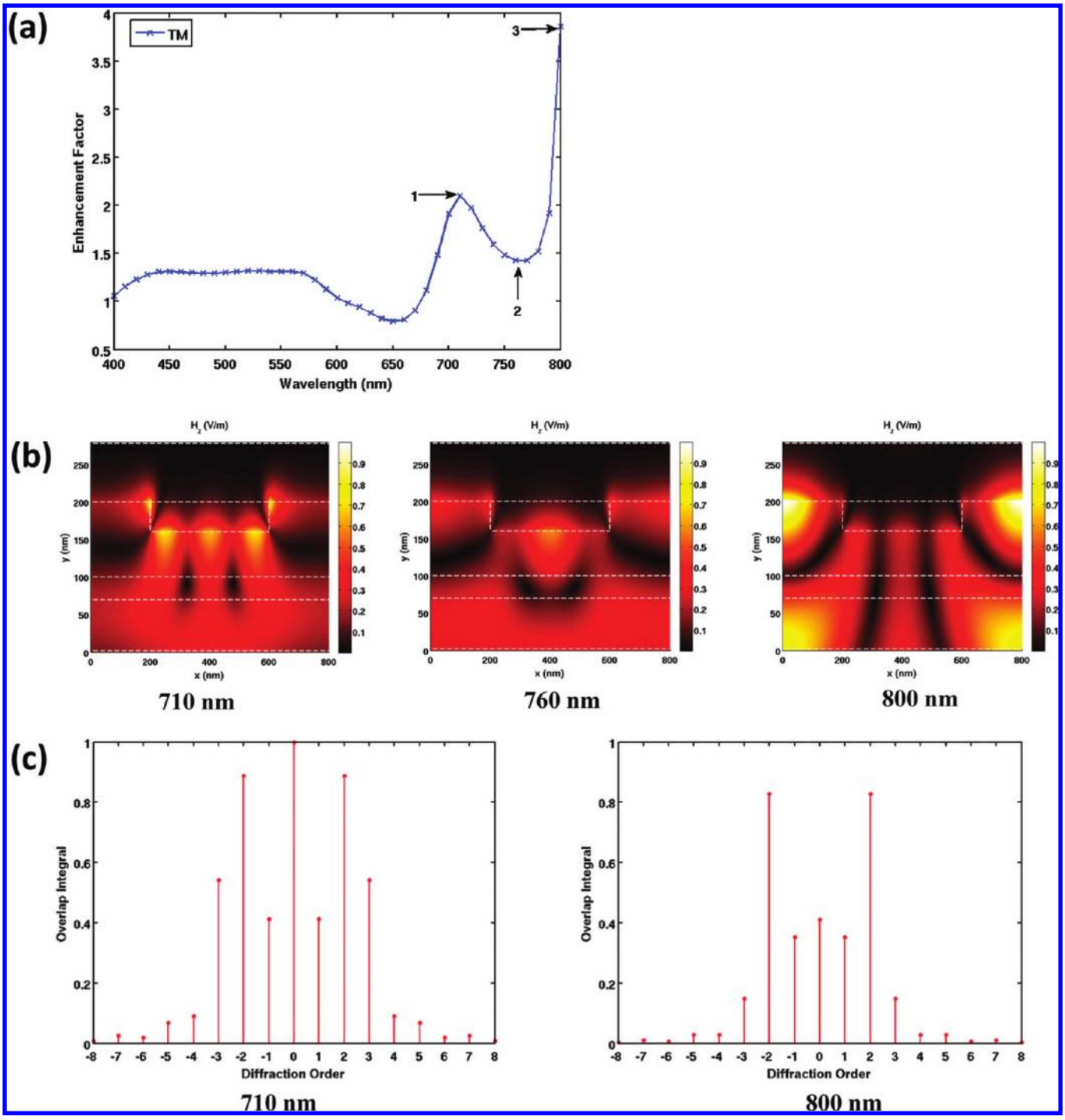

Figure 5. (a) Absorption enhancement of the PSC with the metallic grating compared to that without the metallic grating (control device) for the TM wave at vertical incidence. (b) Near field distributions of the PSC for TM waves at vertical incidences. Figures (i, iii) are the near field distributions of plasmonic band edges corresponding to the peaks 1 and 3 of (a). Figure (ii) is the near field distribution of plasmonic band gap corresponding to the dip 2 of (a). All the figures adopt the same color space for comparisons. (c) The normalized overlap integrals between the near-field distribution of plasmonic band edges and Bloch modes of *m*th diffraction order. The integral domain is limited to the P3HT:PCBM active layer below the metallic gratings peak.

where ε_d and ε_m are permittivities of P3HT:PCBM and Ag, respectively. Particularly, k_{spp} is the dispersion relation of the SPP propagating in the semi-infinite metal−dielectric interface. From the identity, we can easily get that the diffraction order n equals 2 for 800 nm, which is strongly consistent with the overlap integral results. However, the overlap integral for the third-order Bloch mode suddenly increases at 710 nm as comparing the first figure to the second figure in Figure 5(c). If we force the SPP momentum matching condition eq 2 satisfied at 710 nm, then the diffraction order n is calculated to be 2.5 just between integers 2 and 3 (see the first figure in Figure 5(c)). Although we may understand that a kind of hybrid mode from second- and third-order Bloch modes excites the SPP, the explanation ignores the fact that the dispersion relation of SPP in the "semi-infinite"

dx.doi.org/10.1021/jp211237c | J. Phys. Chem. C 2012, 116, 7200−7206

metal−dielectric interface has been perturbed by the periodic grating with modulated refractive indices. A proper momentum matching condition can be revised as

$$k_{spp} + \Delta k_{spp} = k_0 \sin\theta + \frac{2\pi}{P}n$$

where Δk_{spp} is the perturbed momentum by the third-order Bloch mode and $n = 2$ is related to the second-order Bloch mode. The interplay of Bloch modes with second and third diffraction orders not only enable a coupling of SPP to photon energy but also perturb the dispersion relations of SPP opening up a band gap between two plasmonic band edges.

In comparison with previous work[43] arguing that the K-th and $2K$-th Bloch modes open up the band gap in sinusoidally modulated metallic gratings, we found that the plasmonic band edge resonances occur in the squarely modulated metallic grating, resulting from the interplay of second- and third-order Bloch modes. Furthermore, the overlap integral method proposed offers a clear physical understanding to explain the plasmonic band edge resonances. Figure 6 shows the zero-order reflectance of the PSC with the periodic grating by using the rigorous coupled-wave algorithm (RCWA). The theoretical result of the TM wave, which excites SPPs, can well agree with the experimental one with some peak shift caused by nonideal fabrication as shown in the AFM image of the grating. The plasmonic band edge of 710 nm also can match the IPCE result of Figure 3a very well. Another band edge of 800 nm cannot be observed in experiment because the weak absorption of P3HT:PCBM cannot induce significant photocurrents.

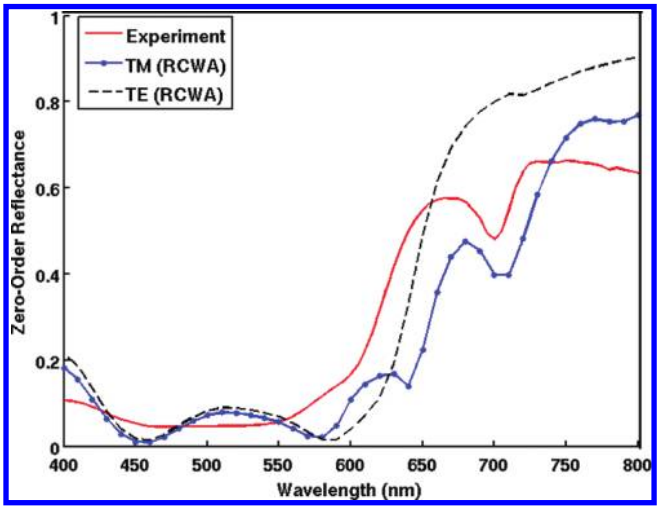

Figure 6. Zero-order reflectance of the PSC with the metallic grating at the incident angle of 15°. The rigorous coupled-wave algorithm (RCWA) is adopted for calculating theoretical results.

Although this work is focused on inverted solar cell structures, the concept is fully adoptable in other solar cells, such as tandem solar cells and polymer−quantum dots hybrid solar cells, which can be beneficial from the plasmonic effects. The fabrication process itself can be in principle scaled up. The nanoimprinted method to fabricate the back grating electrode is highly compatible with the roller painting approach[44,45] in mass producing PSCs. Hence, this method is promising in realizing high-performance polymer solar cells in industrial processes.

CONCLUSIONS

In this study, we have investigated inverted PSCs with a directly patterned active layer and Ag nanograting as the back anode reflector. The resulting nanograting array greatly enhances the light absorption of inverted PSCs through light diffraction and SP modes. As a result, photocurrent results are significantly improved from an IPCE enhancement over a broad wavelength range, with particularly strong peaks at ∼400 nm and 715 nm. Furthermore, the increased FF is another important indicator for the efficient patterned device. As a result, PCE is enhanced from 3.09% to 3.68% upon incorporation of Ag grating. Using the theoretical study, we show that periodic metal grating nanostructure can split the degenerate SPP modes into two plasmonic band edge states with different resonance frequencies, which can significantly enhance the optical absorption of PSC. The work clarifies the physical origin of plasmonic band edge resonance and its role in enhancing the optical absorption of PSCs. As a consequence, besides offering the detailed physics of the optical enhancement, this study demonstrates an effective and simple approach (through adopting a directly patterned active layer to form Ag gratings and appropriate design of layer material and structures) to improve light harvesting of an inverted structure for practical uses.

AUTHOR INFORMATION

Corresponding Author

*E-mail address: chchoy@eee.hku.hk.

Notes

The authors declare no competing financial interest.

ACKNOWLEDGMENTS

This work is supported by UGC grants (#10400897 and #10401466) of the University of Hong Kong, the General Research Funds (HKU#712108 and HKU#712010) from the Research Grants Council of Hong Kong Special Administrative Region, China.

REFERENCES

(1) Arico, A. S.; Bruce, P.; Scrosati, B.; Tarascon, J.-M.; Schalkwijk, W. V. *Nat. Mater.* **2005**, *4*, 366−377.
(2) Gearba, R. I.; Mills, T.; Morris, J.; Pindak, R.; Black, C. T.; Zhu, X. *Adv. Funct. Mater.* **2011**, *21*, 2666−2673.
(3) Tada, A.; Geng, Y.; Wei, Q.; Hashimoto, K.; Tajima, K. *Nat. Mater.* **2011**, *10*, 450−455.
(4) Yuan, Y.; Reece, T. J.; Sharma, P.; Poddar, S.; Ducharme, S.; Gruverman, A.; Yang, Y.; Huang, J. *Nat. Mater.* **2011**, *10*, 296−302.
(5) Chen, L. M.; Hong, Z. R.; Li, G.; Yang, Y. *Adv. Mater.* **2009**, *21*, 1434−1449.
(6) Sun, Y. M.; Seo, J. H.; Takacs, C. J.; Seifter, J.; Heeger, A. J. *Adv. Mater.* **2011**, *23*, 1679−1683.
(7) Steim, R.; Kogler, F. R.; Brabec, C. J. *J. Mater. Chem.* **2010**, *20*, 2499−2512.
(8) Sun, Y.; Wang, M.; Gong, X.; Seo, J. H.; Hsu, B. B. Y.; Wudl, F.; Heeger, A. J. *J. Mater. Chem.* **2011**, *21*, 1365−1367.
(9) Wagner, J.; Gruber, M.; Hinderhofer, A.; Wilke, A.; Bröker, B.; Frisch, J.; Amsalem, P.; Vollmer, A.; Opitz, A.; Koch, N.; et al. *Adv. Funct. Mater.* **2010**, *20*, 4295−4303.
(10) Chen, H.-Y.; Lo, M. K. F.; Yang, G.; Monbouquette, H. G.; Yang, Y. *Nat. Nanotechnol.* **2008**, *3*, 543−547.
(11) Wang, M.; Hu, X.; Liu, P.; Li, W.; Gong, X.; Huang, F.; Cao, Y. *J. Am. Chem. Soc.* **2011**, *133*, 9638−9641.
(12) Davis, R. J.; Lloyd, M. T.; Ferreira, S. R.; Bruzek, M. J.; Watkins, S. E.; Lindell, L.; Sehati, P.; Fahlman, M.; Anthony, J. E.; Hsu, J. W. P. *J. Mater. Chem.* **2011**, *21*, 1721−1729.

(13) Hsieh, C.-H.; Cheng, Y.-J.; Li, P.-J.; Chen, C.-H.; Dubosc, M.; Liang, R.-M.; Hsu, C.-S. *J. Am. Chem. Soc.* **2010**, *132*, 4887−4893.
(14) Ferry, V. E.; Munday, J. N.; Atwater, H. A. *Adv. Mater.* **2010**, *22*, 4794−4808.
(15) Ferry, V. E.; Sweatlock, L. A.; Pacifici, D.; Atwater, H. A. *Nano Lett.* **2008**, *8*, 4391−4397.
(16) Polman, A.; Atwater, H. A. *Nat. Mater.* **2010**, *9*, 205−213.
(17) Baba, A.; Aoki, N.; Shinbo, K.; Kato, K.; Kaneko, F. *ACS Appl. Mater. Interfaces* **2011**, *3*, 2080−2084.
(18) Barnes, W. L.; Dereux, A.; Ebbesen, T. W. *Nature* **2003**, *424*, 824−830.
(19) Wang, C. D.; Choy, W. C. H. *Energy Mater. Sol. Cells* **2011**, *95*, 904−908.
(20) Fung, D. D. S.; Qiao, L. F.; Choy, W. C. H.; Wang, C. D.; Sha, W. E. I.; Xie, F. X.; He, S. L. *J. Mater. Chem.* **2011**, *21*, 16349−16356.
(21) Tvingstedt, K.; Persson, N. K.; Inganas, O.; Rahachou, A.; Zozoulenko, I. V. *Appl. Phys. Lett.* **2007**, *91*, 113514−113516.
(22) Abass, A.; Shen, H. H.; Bienstman, P.; Maes, B. *J. Appl. Phys.* **2011**, *109*, 023111−0231117.
(23) Haug, F. J.; Soderstrom, T.; Cubero, O.; Terrazzoni-Daudrix, V.; Ballif, C. *J. Appl. Phys.* **2008**, *104*, 064509−064516.
(24) Ostfeld, A. E.; Pacifici, D. *Appl. Phys. Lett.* **2011**, *98*, 113112−113114.
(25) Ferry, V. E.; Verschuuren, M. A.; Li, H. B. B. T.; Schropp, R. E. I.; Atwater, H. A.; Polman, A. *Appl. Phys. Lett.* **2009**, *95*, 183503−183505.
(26) Sha, W. E. I.; Choy, W. C. H.; Chew, W. C. *Opt. Lett.* **2011**, *36*, 478−480.
(27) Tumbleston, J. R.; Ko, D. H.; Samulski, E. T.; Lopez, R. *Appl. Phys. Lett.* **2009**, *94*, 043305−043307.
(28) Nalwa, K. S.; Park, J. M.; Ho, K. M.; Chaudhary, S. *Adv. Mater.* **2011**, *23*, 112−116.
(29) Na, S. I.; Kim, S. S.; Jo, J.; Oh, S. H.; Kim, J.; Kim, D. Y. *Adv. Funct. Mater.* **2008**, *18*, 3956−3963.
(30) Wang, D. H.; Kim, D. Y.; Choi, K. W.; Seo, J. H.; Im, S. H.; Park, J. H.; Park, O. O.; Heeger, A. J. *Angew. Chem., Int. Ed.* **2011**, *50*, 5519−5523.
(31) Hsiao, Y.-S.; Chien, F.-C.; Huang, J.-H.; Chen, C.-P.; Kuo, C.-W.; Chu, C.-W.; Chen, P. *J. Phys. Chem. C* **2011**, *115*, 11864−11870.
(32) Ko, D. H.; Turnbleston, J. R.; Schenck, W.; Lopez, R.; Samulski, E. T. *J. Phys. Chem. C* **2011**, *115*, 4247−4254.
(33) Lee, J. H.; Kim, D. W.; Jang, H.; Choi, J. K.; Geng, J.; Jung, J. W.; Yoon, S. C.; Jung, H.-T. *Small* **2009**, *5*, 2139−2143.
(34) Wang, W.; Wu, S. M.; Reinhardt, K.; Lu, Y. L.; Chen, S. C. *Nano Lett.* **2010**, *10*, 2012−2018.
(35) Bai, W. L.; Gan, Q. Q.; Bartoli, F.; Zhang, J.; Cai, L. K.; Huang, Y. D.; Song, G. F. *Opt. Lett.* **2009**, *34*, 3725−3727.
(36) Park, M.; Li, J.; Kumar, A.; Li, G.; Yang, Y. *Adv. Funct. Mater.* **2009**, *19*, 1241−1246.
(37) Moharam, M. G.; Grann, E. B.; Pommet, D. A.; Gaylord, T. K. *J. Opt. Soc. Am. A* **1995**, *12*, 1068−1076.
(38) Ding, I. K.; Zhu, J.; Cai, W. S.; Moon, S. J.; Cai, N.; Wang, P.; Zakeeruddin, S. M.; Gratzel, M.; Brongersma, M. L.; Cui, Y.; et al. *Adv. Energy Mater.* **2011**, *1*, 52−57.
(39) Sha, W. E. I.; Choy, W. C. H.; Chew, W. C. *Opt. Express* **2010**, *18*, 5993−6007.
(40) Haase, C.; Stiebig, H. *Appl. Phys. Lett.* **2007**, *91*, 061116−061118.
(41) Zeng, L.; Yi, Y.; Hong, C.; Liu, J.; Feng, N.; Duan, X.; Kimerling, L. C.; Alamariu, B. A. *Appl. Phys. Lett.* **2006**, *89*, 111111−111113.
(42) http://www.eee.hku.hk/∼wsha/Movie/.
(43) Barnes, W. L.; Preist, T. W.; Kitson, S. C.; Sambles, J. R. *Phys. Rev. B* **1996**, *54*, 6227−6244.
(44) Chanda, D.; Shigeta, K.; Gupta, S.; Cain, T.; Carlson, A.; Mihi, A.; Baca, A. J.; Bogart, G. R.; Braun, P.; Rogers, J. A. *Nat. Nanotechnol.* **2011**, *6*, 402−407.
(45) Jung, J. W.; Jo, W. H. *Adv. Funct. Mater.* **2010**, *20*, 2355−2363.